Journal of Magnetic Resonance 309 (2019) 106601

Contents lists available at ScienceDirect

Journal of Magnetic Resonance

journal homepage: www.elsevier.com/locate/jmr

Diagnosing current distributions in batteries with magnetic resonance imaging

Mohaddese Mohammadi [1], Emilia V. Silletta [1], Andrew J. Ilott, Alexej Jerschow *

Department of Chemistry, New York University, 100 Washington Square East, New York, NY 10003, USA

ARTICLE INFO

Article history:
Received 21 June 2019
Revised 9 September 2019
Accepted 15 September 2019
Available online 16 September 2019

Keywords:
Rechargeable Li-ion batteries
Current distribution
Magnetic Resonance Imaging

ABSTRACT

Batteries and their defects are notoriously difficult to analyze non-destructively, and consequently, many defects and failures remain little noticed and characterized until they cause grave damage. The measurement of the current density distributions inside a battery could reveal information about deviations from ideal cell behavior, and could thus provide early signs of deterioration or failures. Here, we describe methodology for fast nondestructive assessment and visualization of the effects of current distributions inside Li-ion pouch cells. The technique, based on magnetic resonance imaging (MRI), allows measuring magnetic field maps during charging/discharging. Marked changes in the distributions are observed as a function of the state of charge, and also upon sustaining damage. In particular, it is shown that nonlinearities and asymmetries of current distributions could be mapped at different charge states. Furthermore, hotspots of current flow are also shown to correlate with hotspots in charge storage. This technique could potentially be of great utility in diagnosing the health of cells and their behavior under different charging or environmental conditions.

1. Introduction

Nondestructive battery cell testing is of critical importance in employing rechargeable batteries in portable devices, transportation, and in energy storage grids. The accurate prediction of cell and battery lifetime and their capacity fading are of intense interest in many parts of a battery's deployment cycle. There is a lack of fast nondestructive techniques that can provide detailed and localized diagnostic data for fully assembled cells. Here, we describe a Magnetic Resonance Imaging (MRI) based technique that can provide an assessment of current distributions within cells quickly, and is also compatible with many commercial cell designs.

The current distribution within cells is affected by the design and resistance profile of each part of the cell, the heterogeneity of the electrodes, and the type and location of any physical defects such as dendrites or pre-existing cracks [1]. Non-uniform current distributions can be the source of cell failures or capacity loss, often initiated and accompanied by lithium dendrite growth, or assembly imperfections. For example, it was shown that there was a direct correlation between energy density and the non-uniformity of the current distribution, demonstrating a potential to gain as much as 50% in energy density through improving the current distribution [2]. Prior work on measuring current distributions include studies with cell hardware modifications. For example, the implementation of tabs in different positions along the electrodes provided a means of inferring the variability of current [3,4], which demonstrated the significant changes evident in the current, depending on the charge/discharge rate. It is of great interest to perform *in situ* or *operando*, non-invasive, and spatially-resolved measurements of current distributions, as these techniques can pave the way for developing safer and higher performance batteries.

Nuclear magnetic resonance (NMR) and MRI techniques have established themselves as tools for *in situ* and *operando* studies of fundamental cell mechanisms including studies of failure modes, charge storage mechanisms, and ion mobility [5–8]. Stray field NMR studies have been used to map lithium in electrodes [9]. Electron paramagnetic resonance *in situ*/*operando* methodology has been demonstrated for mapping metallic lithium and dendrites [10–12]. Other *in situ*/*operando* methodology include synchrotron-based scanning transmission X-ray microscopy (STXM) [13] and X-ray micro-diffraction [14], energy dispersive X-ray diffraction (EDXRD) [15], X-ray diffraction in combination with other spectroscopic methods such as transmission electron microscopy (TEM) [16,17], operando neutron diffraction [18], operando video microscopy [19], and Raman spectroscopy [20]. All

---

* Corresponding author.
E-mail address: alexej.jerschow@nyu.edu (A. Jerschow).

[1] These authors contributed equally to the work.

https://doi.org/10.1016/j.jmr.2019.106601

these techniques typically require the fabrication of special cells for the study of cell processes.

There are fewer choices of techniques for measuring unaltered commercial-type cells, which have opaque and typically conductive enclosures. Consequently, the amount of information obtainable from such measurements is significantly limited. Notable exceptions include, for example, a fast acoustic method [21,22], electrical measurements [23], and X-ray computed tomography (CT) [24].

In previous work, we have introduced an MRI technique to assess state-of-charge (SOC) via the magnetic fields induced by the magnetic susceptibility of the active cell components, which was based on sensing the induced magnetic field changes of the active materials in the cell [6]. This approach provided fast, nondestructive mapping of SOC and defects. Since the method does not require access to the inside of the cell, it will henceforth be termed inside-out MRI (abbreviated as ioMRI). This ioMRI method is shown here to be suitable for the diagnostics of current distributions within cells as well. A fundamental limitation of applying magnetic resonance techniques to commercial lithium-ion cells is the poor radiofrequency (rf) penetration due to the conductive casing and the electrodes [25,5,26]. The ioMRI technique, however, avoids this complication by simply measuring fields around the device, not within it.

Magnetic fields have been measured for assessing currents before, such as, for example using magneto-optic imaging for studying the flux and current distribution of a long thin strip [27]. MRI-based current imaging was first described by Manassen et al. [28], and this type of methodology is currently being applied *in vivo* for the purpose of electrical property mapping [29–34]. It was also suggested, for example, that neuronal current distributions could be imaged using magnetic resonance imaging [35,31].

In this article, we demonstrate a technique for assessing current distributions within commercial-type Li-ion pouch cells. Experiments were performed with different discharging/charging current rates on healthy and mechanically stressed cells. Marked differences were observed as a function of state of charge (SOC) and after stressing the cell. It is also demonstrated that the current distribution can be significantly asymmetric when switching from charge to discharge current, the current distribution may be nonlinear with respect to overall applied current, and that there appears to be an interesting symmetry between states at full charge and near full discharge.

2. Experimental

2.1. Cells

Stacked electrode Li-ion pouch cells were used for imaging. Multilayer stacked electrode cells were manufactured as described previously [6] at the battery prototyping center at Rochester Institute of Technology (RIT) with a capacity of 250 mAh and a nominal voltage of 3.7 V. The materials that were used for the cell construction were $Li_{1.02}Ni_{0.50}Mn_{0.29}Co_{0.19}O_2$ as the cathode, Graphite as the anode and 1.2 M $LiPF_6$ EC:DMC 3:7 as the electrolyte. For increasing the conductivity and structure of working electrodes powder grade carbon black and PVDF were used.

2.2. Battery holders

Cylindrical holders with 39-mm diameter were designed in Tinkercad and 3D printed with a Polylactic Acid (PLA) filament. The holders were filled with a 15 mM $CuSO_4$ solution in water, giving a ^1H T_1 relaxation constant of 100 ms.

2.3. Cycling conditions

In order to fully charge cells (up to voltage 4.2 V), cells were first charged with a current of 25 mA (0.1C). Then, for each step of SOC, RIT cells were discharged with 125 mA (0.5C) until the cell reached 2.5 V. Cells were always operated between 4.2 V and 2.5 V. During current imaging, the cell was charging and discharging with a constant current protocol using a Biologic VSP potentiostat. The cycler remained connected to the cell throughout all measurements. An aluminum foil and an in-line low-pass filter with cutoff frequency of 1.9 MHz were used to shield the probe area from rf interference. Cells were precycled for 5–7 full cycles to bring them to a stable state after storage.

2.4. Magnetic Resonance Imaging

A 9.4 T Bruker Ultrashield Avance I spectrometer with a Bruker mini0.75 gradient assembly was used for performing the MRI experiments. The resonance frequency of ^1H in the spectrometer was 400.1 MHz. For imaging and data collection, a Bruker MiniWB57 imaging probe was used with a Bruker WB57 40-mm i.d. coil insert for ^1H experiments.

A slice selective 2D fast low angle shot (FLASH) sequence with nominal flip angle (α) of 15°, Repetition Time (TR) of 100 ms, 12 scans of averaging, and four different echo times of 2.45, 2.5, 2.75, and 2.80 ms were used to acquire the 2D ^1H images. The readout direction was along z while x was the phase-encoded dimension and 128 points were collected along each dimension. The field of view (FOV) was 51.2 mm in the x and z-direction, which resulted in a 400 μm resolution. The slice thickness was 1 mm. Each 2D experiment took approximately 2.5 min.

2.5. Calculations

Finite Element calculations were performed with COMSOL Multiphysics with the AC/DC module. A stacked-electrode cell and a cell model with one jelly roll were created in COMSOL (a calculation for a jelly-rolled cell yielded similar results). The calculation utilized the AC/DC module and solved Ampere's Law with current conservation boundary conditions.

The model of the stacked-cut electrode battery was composed of two single-sided coated anodes, one double-sided coated cathode, two aluminum current collectors, one copper current collector and three tabs for positive and negative ports. A mesh of 11,930,062 elements was used for finite element analysis. In the simulation of the charging/discharging condition, the copper tab of the battery was assigned as the positive/negative constant current terminal and the aluminum tabs were always grounded. Supplementary Fig. S3 shows a depiction of the model.

The phase map was calculated from phase images using an unwrapping algorithm as described previously [6].

3. Results and discussion

Cells were placed in a slot in a custom-designed holder, containing compartments for water, as described previously [6]. For the measurements reported here a 15 mM CuSO4 water solution was used as the detection medium in order to shorten the T_1 relaxation time constant and thus allow faster imaging. The arrangement used is illustrated in Fig. 1A. The MRI signals were obtained from the water compartment and all represented images in this article originated from a slice mid-way across the cell as indicated in Fig. 1A. The measurement was based on a slice-selective FLASH imaging sequence, with different echo times. The different echo times allowed encoding the precession angles, from which the

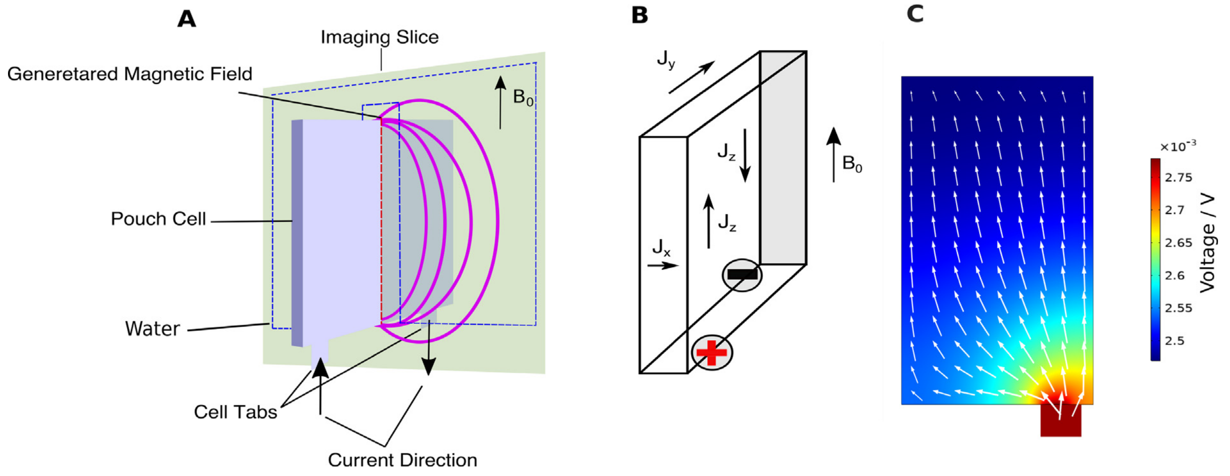

Fig. 1. Illustration of the experimental arrangement and measured quantities. (A) Cell position and orientation of imaging slice, as well as indication of the detected volume (dashed rectangle). (B) Current distribution elements inside the battery and cell orientation. (C) Calculated current and voltage distribution on the positive current collector during charging.

local precession frequency could be obtained accurately. After phase unwrapping, magnetic field images were produced. Only currents perpendicular to the static magnetic field led to observable fields, as the spin precession is only significantly affected by magnetic field components collinear with B_0. The orientations of the different coordinate axes are indicated in Fig. 1B.

Fig. 1C shows the results from a current distribution calculation, considering an ideal rectangular electrode assembly (as shown in Fig. S3) and negligible effects from non-uniform charge states. The current pattern for both the positive and negative electrodes looks the same in this calculation, except that the polarity is reversed. The current distribution resembles those previously determined by theoretical and computational means [36].

To explore the effect of the SOC on the current distribution, a cell made with 5 stacked double-coated cathode/anode layers, was first fully charged to 4.2 V, and then measured after discharging it by the specific amounts shown in Fig. 2. The measurements were performed while either discharge or charge current was applied around the indicated depth of discharge (DOD). From each obtained field map, a reference image at the same DOD, acquired during the resting period (no current flow) was subtracted. This process was essential, because at the magnetic field used (9.4 T), and in the chosen current regimes, the susceptibility effect was much stronger than the effect produced by the current (in Fig. S1, the effect of susceptibility at different SOC is shown). It is seen in Fig. 2 that a significant change in the current-produced magnetic fields is observed at the different DOD for both charge and discharge current.

Generally, the highest fields observed are near the tab, which is expected. As the DOD increases, maxima develop in other locations, in particular also at the opposite end (top of the cell). This aspect is particularly interesting, as this phenomenon is related to a nonuniformity in SOC across the cathode. It is useful to compare these results with the resting images shown in Fig. S1. As described previously, these images can be interpreted as showing mostly a distribution of the SOC across the cathode (for this battery material) [6]. As the cathode material is enriched with lithium more and more, the magnetic susceptibility increases and the effect on the magnetic field increases as well. It is seen that 'hot spots' shown in Fig. 2 also appear as spots of maxima in Fig. S1, thus indicating that current flow is correlated with areas of highest susceptibility and thus areas of highest DOD.

It is of note that there appears to be no strict symmetry between maps for charge and discharge current at the same DOD, i.e. current is not simply reversed. This could be explained in the following way: for example, at low DOD (near full charge), there is only a small fraction of active material that is able to accept the charge, and it is much more dispersed, while during the discharge operation, current can be drawn from most charged areas. A similarly large asymmetry is observed for the highest DOD case: in this situation, during discharge, there are few areas that can produce current easily from the stored charge, while there are many more areas that can accept current during charging.

The two extreme cases, high and low DOD, however, observe an interesting symmetry when considered together. In the magnetic field histograms (Fig. 2) for the lowest DOD, one can see only one single peak for the field from discharge current and two peaks (positive/negative) for charge current. For the highest DOD, the situation is reversed: a single peak is observed for charge current and two peaks for discharge current. The flip in sign for overall current is relatively straightforward to understand – the direction of the current is reversed. With regard to the difference between a single peak or a double peak, one can suggest the following explanation: Considering that a more or less uniform current is flowing along the *y*-direction, one would expect the magnetic field to be positive on one side of the cell and negative on the other, which would generate a double-peaked distribution. At low DOD, during charging, current is only weakly perturbed by the influence of active material, because the majority of the material is saturated. A similar situation is encountered for high DOD during discharge current – little active material is available to provide strong non-uniform perturbations in the current. Hence, in these two situations, one would expect a double-peaked distribution, centered around zero field, as was indeed observed.

A simulation was performed in order to explore this last point: the calculation was performed in a cell model while neglecting the contribution of active material. The model for this calculation is shown in Fig. S3. The result is shown in the bottom right panel of Fig. 2. The calculation shows the clear emergence of a double peak. The magnetic field range predicted is also in the same numerical range as shown in the experiments. The inner sharp peaks arise from areas further away from the cell, which may not be included in the experiment. Furthermore, the histogram also shows significant areas of very high positive and negative fields. These areas correspond to regions that are very close to the cell and may result in signal cancellation due to partial volume effects, and would thus not be observable in the experiment. Further minor differences may be due to the fact that the simulation did

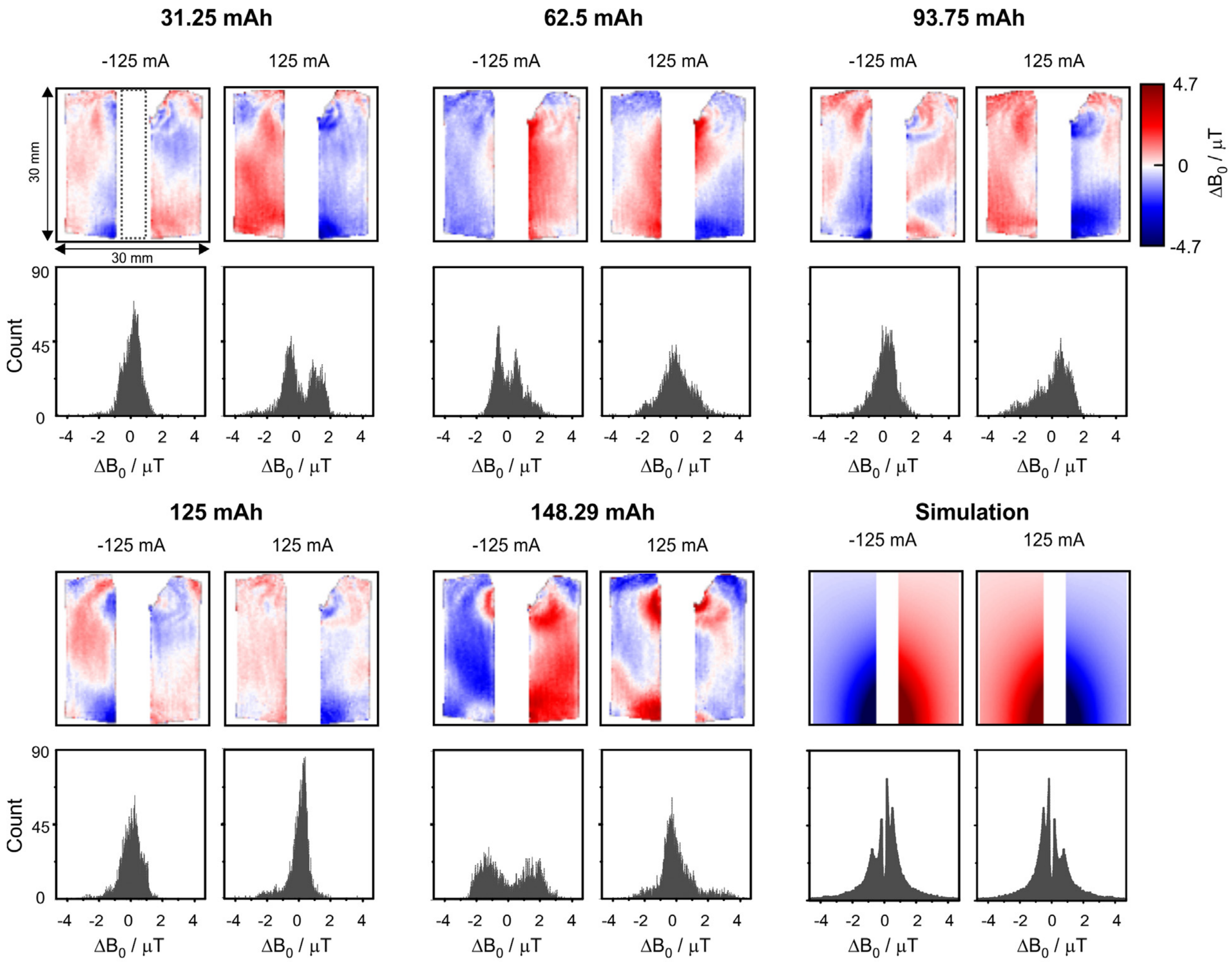

Fig. 2. Magnetic field maps and histograms during discharge (negative current) and charge (positive current) at different depth of discharge (DOD) as indicated. The maps were obtained after subtracting a reference image from the resting period between discharging and charging at each DOD. A constant background field was further subtracted to reduce effects of magnet field drifts. The bottom right panel shows a simulation. The battery leads in these measurements are located at the bottom of each map. The discharge capacity is indicative of the starting point of each step, and discharge measurements were performed before charge measurements. The imaging dimensions and the location of the cell (dotted rectangle) are indicated in the top left image.

not incorporate any SOC inhomogeneities. Overall, there is hence a good conceptual agreement between this model calculation and the experiments in the regimes described above (at maximum and minimum DOD).

In order to investigate the effect of current further, experiments were performed at full SOC (i.e. DOD = 0 mAh) with different overall currents used for discharge and charge operation (see Fig. 3). The histogram clearly shows that the double-peak pattern develops only above a certain threshold current (75 mA), is strongest at 125 mA, and remains absent for negative current (discharging), which is in line with the discussion in relation to Fig. 2. This effect could be rationalized by considering that a smaller current is affected more by perturbations from the active material. An error analysis of the data acquisition was performed by imaging the cell at its resting period for four times with a time interval of 1 h. The standard deviation map is shown in Fig. S2 (0.088 ppm, corresponding to 0.827 µT). This assessment would indicate that for this setup currents below a charge/discharge current of 100 mA are challenging to monitor with high precision.

In order to further examine the regimes of linearity of field vs. applied current, an analysis was performed to fit a linear model on a voxel-by-voxel basis to the magnetic field produced as a function of overall applied current. Fig. 4A shows the results for the slope (field per unit current) if the maps obtained for all currents (positive and negative) are used for the fit. Deviations from linearity were clearly visible in many data points.

In order to provide a quantitative test for overall linearity, different combinations of maps were used for the fit, and the average root-mean-square deviation in the linear fit for each pixel was calculated across the whole measurement volume (Fig. 4B). It is seen that the deviation from linear behavior was largest if data from all measured current regimes were used. The largest deviation could be traced to originate from the negative current points (see the first two bars in Fig. 4B, which have similarly high root-mean-square deviation values). The smallest deviation was found when only the three highest current regimes were used, and it was only slightly larger if the 50 mA point was included. This finding highlights a potential deviation from linear behavior for the discharge regime. This result would be in line with earlier arguments that near full SOC, the discharge current experiences significant contributions from the active material, whereby the current distribution would be significantly altered. During charge, however, current flows more uniformly, and the active material does not produce significant inhomogeneities in the measurement.

Finally, it is demonstrated that the current distribution is significantly altered when a cell is damaged. Fig. 5 shows the magnetic field histograms after damaging the cell by dropping a 245 g rod, with 1 cm diameter from a height of 30 cm, resulting in an energy

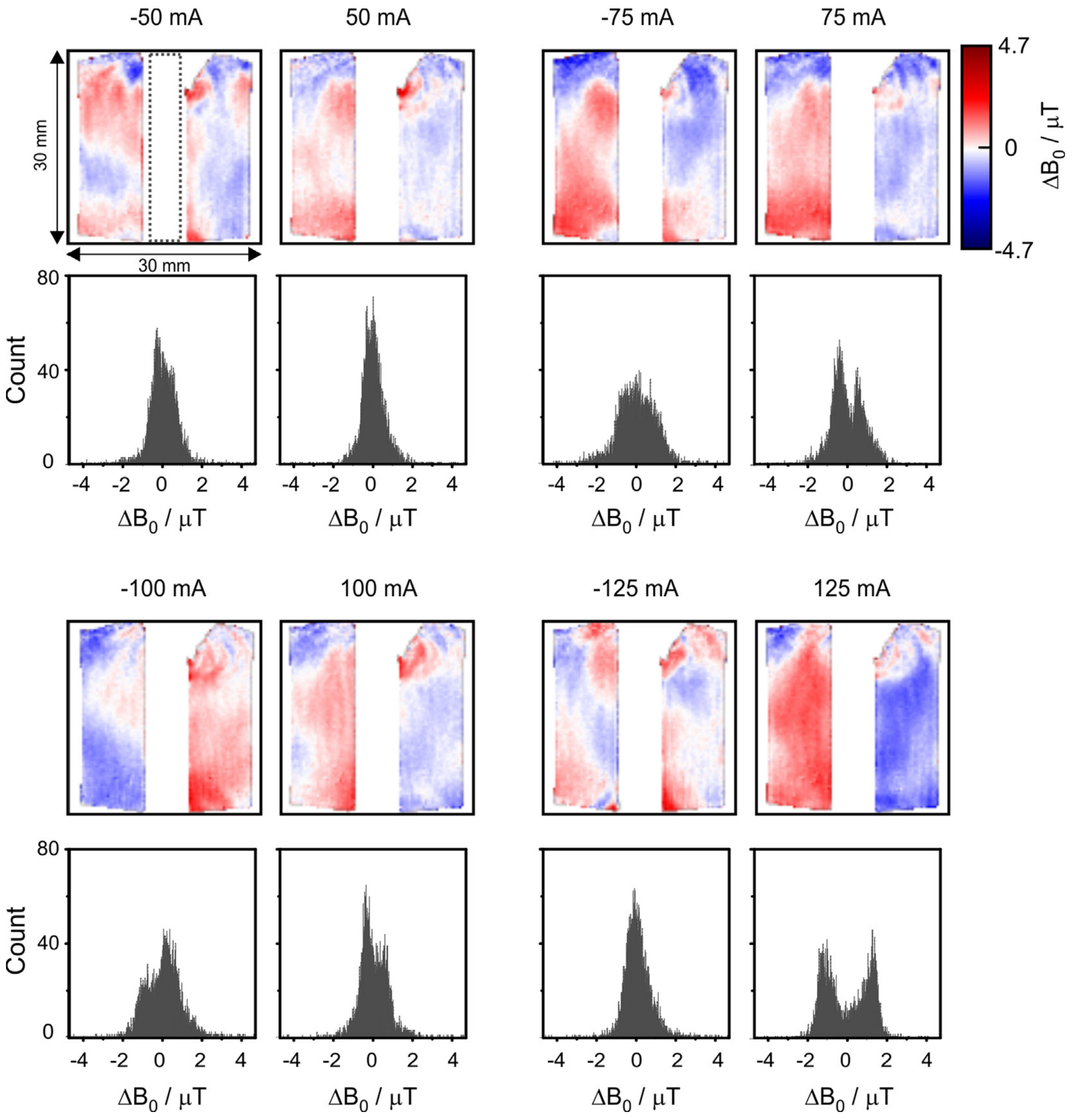

Fig. 3. Magnetic field maps and histograms as a function of overall discharge/charge current near full charge (DOD = 0 mAh). Reference image and background field subtraction was performed in the same way as for Fig. 2. The imaging dimensions and the location of the cell (dotted rectangle) are indicated in the top left image.

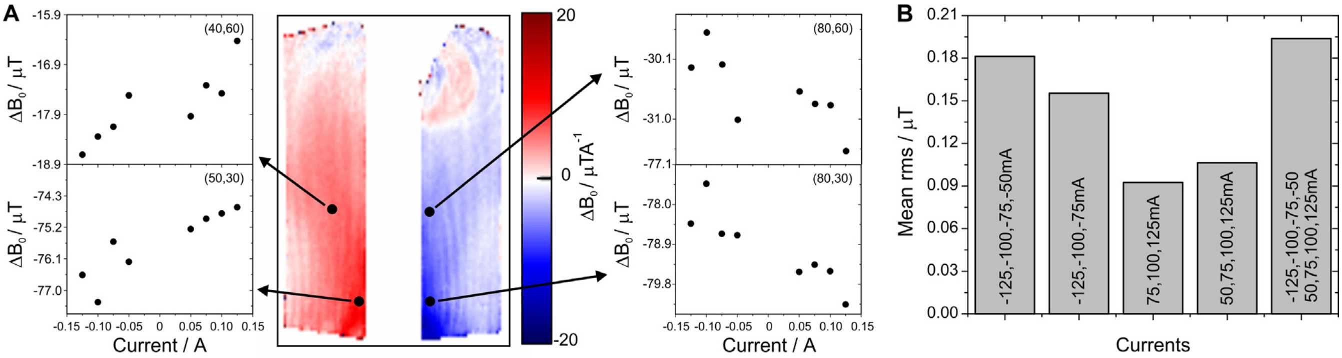

Fig. 4. (A) In the center, the spatially resolved map shows the result of a linear per-voxel fit of magnetic field vs. current, using all the current regimes measured (−125, −100, −75, −50, 50, 75, 100, 125 mA). Several points are extracted for illustration only, showing the magnetic field vs. current at each location. (B) Overall root mean square deviation of the linear fits across the whole volume performed by using the different data combinations as indicated.

released per unit area of 9175.79 J/m^2. Pictures of the drop-rod system and damaged cell are shown in Figs. S4 and S5. The damage led to significant changes in the current distribution, as is clearly observed in Fig. 5.

4. Conclusion

In summary, we have demonstrated here an MRI-based technique for the nondestructive assessment of current distributions

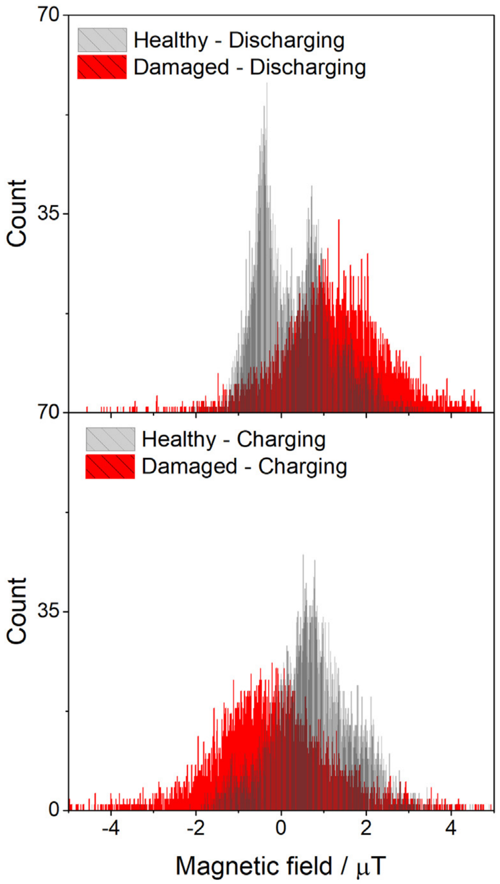

Fig. 5. Histograms calculated from the magnetic field maps during discharging and charging for a damaged cell at 62.5 mAh DOD (after subtracting a reference image in the resting state).

within rechargeable Li-ion cells. The technique, referred to as an "inside-out" MRI approach (ioMRI), pointed to an asymmetry in the current distributions between charging and discharging, which evolved as a function of SOC. The behavior near full SOC during charge operation and at high DOD during discharge operation demonstrated a notable similarity, which could be indicative of less localized and less pronounced perturbations from the active material. Indications for overall non-linearities in the current distributions were observed as well. Hotspots in current distribution also roughly coincided with hotspots in charge storage, although additional detailed studies would be required to quantify these findings further. Damages to the cell showed marked changes in current distributions as well. This measurement methodology could be promising for quick noninvasive assessment of cell behavior during charging and discharging and for determining the evolution of cell behavior.

Acknowledgements

Funding was provided by grants from the US National Science Foundation under programs CBET 1804723 and PFI-TT 1827585. We acknowledge the support from the Battery Prototyping Center team at the Rochester Institute of Technology (RIT), Dr. Matthew Ganter and Dr. Christopher Schauerman.

Author contributions

M.M and E.V.S contributed equally to the work. M.M, A.J. and A. J.I. designed the experiments. M.M. carried out the experiments and simulations. E.V.S performed the calculation and generated images. M.M, E.V.S and A.J. analyzed the results and wrote the paper.

Declaration of Competing Interest

The authors declare no competing interests.

Appendix A. Supplementary material

Supplementary data to this article can be found online at https://doi.org/10.1016/j.jmr.2019.106601.

References

[1] D.R. Baker, M.W. Verbrugge, Temperature and current distribution in thin-film batteries, J. Electrochem. Soc. 146 (1999) 2413–2424.
[2] G. Zhang, C.E. Shaffer, C.-Y. Wang, C.D. Rahn, Effects of non-uniform current distribution on energy density of li-ion cells, J. Electrochem. Soc. 160 (2013) A2299–A2305.
[3] A. Samba, N. Omar, H. Gualous, O. Capron, P. Van den Bossche, J. Van Mierlo, Impact of tab location on large format lithium-ion pouch cell based on fully coupled tree-dimensional electrochemical-thermal modeling, Electrochim. Acta 147 (2014) 319–329.
[4] G. Zhang, C.E. Shaffer, C.-Y. Wang, C.D. Rahn, In-situ measurement of current distribution in a li-ion cell, J. Electrochem. Soc. 160 (2013) A610–A615.
[5] A.J. Ilott, M. Mohammadi, H.J. Chang, C.P. Grey, A. Jerschow, Real-time 3D imaging of microstructure growth in battery cells using indirect MRI, Proc. Natl. Acad. Sci. 113 (2016) 10779–10784.
[6] A.J. Ilott, M. Mohammadi, C.M. Schauerman, M.J. Ganter, A. Jerschow, Rechargeable lithium-ion cell state of charge and defect detection by in-situ inside-out magnetic resonance imaging, Nat. Commun. 9 (2018) 1776.
[7] A.J. Ilott, N.M. Trease, C.P. Grey, A. Jerschow, Multinuclear *in situ* magnetic resonance imaging of electrochemical double-layer capacitors, Nat. Commun. 5 (2014) 4536.
[8] H.J. Chang, A.J. Ilott, N.M. Trease, M. Mohammadi, A. Jerschow, C.P. Grey, Correlating microstructural lithium metal growth with electrolyte salt depletion in lithium batteries using 7Li MRI, J. Am. Chem. Soc. 137 (2015) 15209–15216.
[9] J.A. Tang, S. Dugar, G. Zhong, N.S. Dalal, J.P. Zheng, Y. Yang, R. Fu, Non-destructive monitoring of charge-discharge cycles on lithium ion batteries using ^{7}Li stray-field imaging, Sci. Rep. 3 (2013) srep02596.
[10] Arvid Niemöller, Peter Jakes, Rüdiger-A. Eichel, Josef Granwehr, EPR imaging of metallic lithium and its application to dendrite localisation in battery separators, Sci. Rep. 8 (1) (2018), https://doi.org/10.1038/s41598-018-32112-y.
[11] J. Wandt, C. Marino, H.A. Gasteiger, P. Jakes, R.-A. Eichel, J. Granwehr, Operando electron paramagnetic resonance spectroscopy – formation of mossy lithium on lithium anodes during charge–discharge cycling, Energy Environ. Sci. 8 (2015) 1358–1367.
[12] M. Sathiya, J.-B. Leriche, E. Salager, D. Gourier, J.-M. Tarascon, H. Vezin, Electron paramagnetic resonance imaging for real-time monitoring of Li-ion batteries, Nat. Commun. 6 (2015) 6276.
[13] J. Lim, Y. Li, D.H. Alsem, H. So, S.C. Lee, P. Bai, D.A. Cogswell, X. Liu, N. Jin, Y. Yu, N.J. Salmon, D.A. Shapiro, M.Z. Bazant, T. Tyliszczak, W.C. Chueh, Origin and hysteresis of lithium compositional spatiodynamics within battery primary particles, Science 353 (2016) 566–571.
[14] J. Liu, M. Kunz, K. Chen, N. Tamura, T.J. Richardson, Visualization of charge distribution in a lithium battery electrode, J. Phys. Chem. Lett. 1 (2010) 2120–2123.
[15] W.A. Paxton, Z. Zhong, T. Tsakalakos, Tracking inhomogeneity in high-capacity lithium iron phosphate batteries, J. Power Sources 275 (2015) 429–434.
[16] M. Morcrette, Y. Chabre, G. Vaughan, G. Amatucci, J.-B. Leriche, S. Patoux, C. Masquelier, J.-M. Tarascon, In situ X-ray diffraction techniques as a powerful tool to study battery electrode materials, Electrochim. Acta 47 (2002) 3137–3149.
[17] J.-H. Cheng, A.A. Assegie, C.-J. Huang, M.-H. Lin, A.M. Tripathi, C.-C. Wang, M.-T. Tang, Y.-F. Song, W.-N. Su, B.J. Hwang, Visualization of lithium plating and stripping via in operando transmission X-ray microscopy, J. Phys. Chem. C 121 (2017) 7761–7766.
[18] S. Taminato, M. Yonemura, S. Shiotani, T. Kamiyama, S. Torii, M. Nagao, Y. Ishikawa, K. Mori, T. Fukunaga, Y. Onodera, T. Naka, M. Morishima, Y. Ukyo, D. S. Adipranoto, H. Arai, Y. Uchimoto, Z. Ogumi, K. Suzuki, M. Hirayama, R. Kanno, Real-time observations of lithium battery reactions—operando neutron diffraction analysis during practical operation, Sci. Rep. 6 (2016) 28843.
[19] K.N. Wood, E. Kazyak, A.F. Chadwick, K.-H. Chen, J.-G. Zhang, K. Thornton, N.P. Dasgupta, Dendrites and pits: untangling the complex behavior of lithium metal anodes through operando video microscopy, ACS Cent. Sci. 2 (2016) 790–801.

[20] J.-C. Panitz, P. Novák, O. Haas, Raman microscopy applied to rechargeable lithium-ion cells-steps towards in situ Raman imaging with increased optical efficiency, Appl. Spectrosc. 55 (2001) 1131–1137.

[21] A.G. Hsieh, S. Bhadra, B.J. Hertzberg, P.J. Gjeltema, A. Goy, J.W. Fleischer, D.A. Steingart, Electrochemical-acoustic time of flight: in operando correlation of physical dynamics with battery charge and health, Energy Environ. Sci. 8 (2015) 1569–1577.

[22] G. Davies, K.W. Knehr, B.V. Tassell, T. Hodson, S. Biswas, A.G. Hsieh, D.A. Steingart, State of charge and state of health estimation using electrochemical acoustic time of flight analysis, J. Electrochem. Soc. 164 (2017) A2746–A2755.

[23] R. Petibon, C.P. Aiken, N.N. Sinha, J.C. Burns, H. Ye, C.M. VanElzen, G. Jain, S. Trussler, J.R. Dahn, Study of electrolyte additives using electrochemical impedance spectroscopy on symmetric cells, J. Electrochem. Soc. 160 (2013) A117–A124.

[24] D.P. Finegan, M. Scheel, J.B. Robinson, B. Tjaden, I. Hunt, T.J. Mason, J. Millichamp, M. Di Michiel, G.J. Offer, G. Hinds, D.J.L. Brett, P.R. Shearing, *In-operando* high-speed tomography of lithium-ion batteries during thermal runaway, Nat. Commun. 6 (2015) 6924.

[25] A.J. Ilott, S. Chandrashekar, A. Klöckner, H.J. Chang, N.M. Trease, C.P. Grey, L. Greengard, A. Jerschow, Visualizing skin effects in conductors with MRI: 7Li MRI experiments and calculations, J. Magn. Reson. 245 (2014) 143–149.

[26] A.J. Ilott, A. Jerschow, Super-resolution surface microscopy of conductors using magnetic resonance, Sci. Rep. 7 (2017) 5425.

[27] T.H. Johansen, M. Baziljevich, H. Bratsberg, Y. Galperin, P.E. Lindelof, Y. Shen, P. Vase, Direct observation of the current distribution in thin superconducting strips using magneto-optic imaging, Phys. Rev. B Condens. Matter 54 (1996) 16264–16269.

[28] Y. Manassen, E. Shalev, G. Navon, Mapping of electrical circuits using chemical-shift imaging, J. Magn. Reson. 1988 (76) (1969) 371–374.

[29] M. Joy, G. Scott, M. Henkelman, In vivo detection of applied electric currents by magnetic resonance imaging, Magn. Reson. Imaging 7 (1989) 89–94.

[30] D.S. Tuch, V.J. Wedeen, A.M. Dale, J.S. George, J.W. Belliveau, Conductivity tensor mapping of the human brain using diffusion tensor MRI, Proc. Natl. Acad. Sci. 98 (2001) 11697–11701.

[31] M.L.G. Joy, V.P. Lebedev, J.S. Gati, Imaging of current density and current pathways in rabbit brain during transcranial electrostimulation, IEEE Trans. Biomed. Eng. 46 (1999) 1139–1149.

[32] X. Zhang, S. Zhu, B. He, Imaging electric properties of biological tissues by RF field mapping in MRI, IEEE Trans. Med. Imaging 29 (2010) 474–481.

[33] A.L.H.M.W. van Lier, D.O. Brunner, K.P. Pruessmann, D.W.J. Klomp, P.R. Luijten, J.J.W. Lagendijk, C.A.T. van den Berg, B Phase mapping at 7 T and its application for in vivo electrical conductivity mapping, Magn. Reson. Med. 67 (2012) 552–561.

[34] J. Shin, M.J. Kim, J. Lee, Y. Nam, M. Kim, N. Choi, S. Kim, D.-H. Kim, Initial study on in vivo conductivity mapping of breast cancer using MRI, J. Magn. Reson. Imaging 42 (2015) 371–378.

[35] N.W. Halpern-Manners, V.S. Bajaj, T.Z. Teisseyre, A. Pines, Magnetic resonance imaging of oscillating electrical currents, Proc. Natl. Acad. Sci. 107 (2010) 8519–8524.

[36] P. Taheri, A. Mansouri, M. Yazdanpour, M. Bahrami, Theoretical analysis of potential and current distributions in planar electrodes of lithium-ion batteries, Electrochim. Acta 133 (2014) 197–208.